ST-CDM MIMO Radar Imaging with Sparse Linear Arrays

Hangyu Liu, Xiaolei Shang, and Ronghao Lin

***Abstract*—We consider significantly enhancing the angular resolution of a single-chip multiple-input multiple-output (MIMO) radar sensor equipped with only 3 transmit and 4 receive antennas for radar imaging. We adopt the slow-time code-division multiplexing (ST-CDM) transmission scheme, which is a low-cost viable option to attain a large virtual array without reducing the unambiguous Doppler range. Moreover, to significantly improve the angular resolution without increasing antenna numbers, we introduce a practical 3×4 sparse linear array (SLA) design. We extend the iterative adaptive approach (IAA) to the slow-time IAA (ST-IAA) algorithm, aiming to mitigate the impact of waveform separation residuals and the high angular sidelobes on ST-CDM MIMO radar imaging equipped with SLAs. Furthermore, we construct a single-chip ST-CDM MIMO radar prototype with the 3×4 SLA design for experimental validations. The numerical and experimental results are provided to demonstrate the enhanced imaging performance of the radar prototype when used with the ST-IAA algorithm.**

***Index Terms*—Multiple-input multiple-output (MIMO) radar, slow-time code-division multiplexing (ST-CDM), sparse linear array (SLA), single-chip radar sensor, iterative adaptive approach (IAA), slow-time IAA (ST-IAA)**

I. Introduction

MULTIPLE-INPUT multiple-output (MIMO) radar has become a standard in diverse applications due to its cost-effectiveness and power efficiency [1] [2]. The MIMO framework enables the formation of a large virtual array with $M \times N$ elements using M transmit and N receive antennas, resulting in enhanced angular resolution using fewer physical antennas and fewer receive channels compared to traditional radar systems. Achieving waveform orthogonality at the transmitters is a crucial aspect of attaining the large MIMO virtual array. For popular linear frequency-modulated continuous-wave (LFMCW) MIMO radars, the primary methods to achieve waveform orthogonality are time-division multiplexing (TDM), Doppler-division multiplexing (DDM), and slow-time code-division multiplexing (ST-CDM) [3].

ST-CDM exhibits significant advantages over its TDM and DDM counterparts. As shown in Fig. 1, each transmitter of TDM emits a probing waveform alternatingly, whereas all transmitters of DDM and ST-CDM emit waveforms simultaneously. Although TDM has the advantages of convenient hardware configuration and signal processing, DDM and ST-CDM allow higher radiation power [4] due to the simultaneous signal emissions. Moreover, unlike TDM, they do not suffer from virtual array distortions caused by the motion-induced Doppler shifts [5]. Furthermore, the pulse repetition interval (PRI) T_{PRI} of TDM is M times that of the simultaneous transmission methods. Since the maximum unambiguous detectable velocity

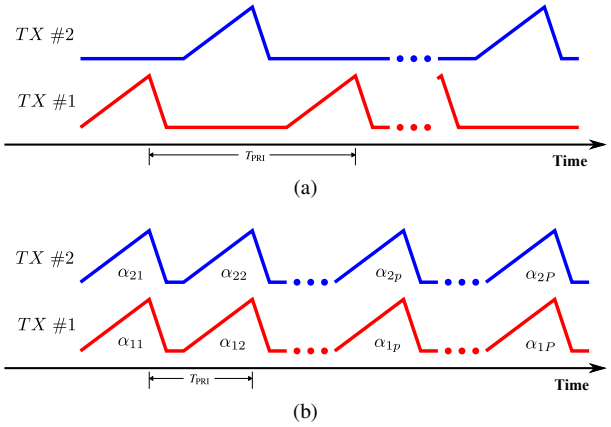

Fig. 1. An example of LFMCW waveforms in a coherent processing interval (CPI) transmitted by a MIMO radar with two transmit channels. (a) TDM: each transmit channel is switched on and off alternatingly. (b) DDM and ST-CDM: all transmit channels transmit simultaneously utilizing different phase codes from one period to another (over slow-time).

[6] $v_{\max}$ is inversely proportional to T_{PRI}, $v_{\max}$ of TDM is reduced by a factor of M. Waveform orthogonality of DDM and ST-CDM is achieved through the multiplication of each slow-time waveform (i.e., from one PRI to another) within a coherent processing interval (CPI) with a phase code. The phase codes of DDM shift different transmit signals to different zones of the Doppler spectrum [7]. Despite the convenient waveform separation through band-pass filters (BPF) over slow-time, DDM suffers from the same drawback of reduced $v_{\max}$ as TDM, by a factor of M. In comparison, ST-CDM exhibits superior spectral efficiency by using spreading codes over slow-time and avoids the reduction of $v_{\max}$, rendering it a more suitable option for many MIMO radar applications [8].

Besides employing ST-CDM for trying to achieve waveform orthogonalization, it is also essential to consider using sparse linear arrays (SLAs) [9] [10] to significantly enhance the angular resolution for MIMO radar imaging. Owing to cost and size constraints, current MIMO radar sensors are typically equipped with a single transceiver chip [11]. For instance, the AWR2243 radar chip [12] from Texas Instruments (TI) has 3 transmit channels and 4 receive channels. As a result, the single-chip radar sensors equipped with AWR2243 consist of only 3 transmit antennas and 4 receive antennas. If such a single-chip sensor adopts a simple 3×4 uniform linear array (ULA) design, the angular resolution of the virtual array is limited to approximately 8.5°, making it a challenge to distinguish adjacent targets at relatively long distances. The SLAs can increase the array aperture without adding more antennas, thereby achieving

higher angular resolution, which is particularly beneficial for currently available single-chip MIMO radar sensors.

In summary, the ST-CDM MIMO radar with SLAs offers the advantages of larger unambiguous Doppler range and much higher angular resolution than their TDM/DDM and ULA counterparts. However, both ST-CDM and SLAs introduce significant challenges to high quality radar imaging. On the one hand, the imperfect waveform separation [13], such as the conventional matched filtering (MF), can result in each separated transmit signal of the ST-CDM radar being contaminated by unwanted interference from other transmit channels, leading to the presence of strong "waveform separation residuals". These residuals manifest as high sidelobes in the Doppler spectra of radar imaging. On the other hand, due to the array aperture enlargement with a small number of antennas, the SLAs tend to exhibit high sidelobes [14] in the angular spectra of radar imaging when using conventional beamforming.

To attain high quality imaging performance using the ST-CDM MIMO radar with SLAs, we need to mitigate the aforementioned two categories of high sidelobes. In the field of spectral estimation, the nonparametric iterative adaptive approach (IAA) [15]–[17] is a classic hyperparameter-free algorithm, which can process diverse experimentally measured data without the need to tune user parameters. The IAA algorithm not only exhibits strong robustness similar to the conventional MF method, but also has the capability to achieve super-resolution and low sidelobe levels with a single snapshot, making it suitable for the highly dynamic environment [18]. These advantages have made IAA receive increasing attention in recent years [19]–[21]. We extend the IAA algorithm based on the signal model of the ST-CDM MIMO radar with SLAs, enabling the high quality Doppler-angle imaging and hence the accurate estimation of Doppler and angular information of targets. The extended algorithm is referred to as the slow-time IAA (ST-IAA) algorithm, which has been preliminarily investigated in our recent work [22]. There are several other well-known hyperparameter-free algorithms that can be extended in a similar manner for use in ST-CDM, such as sparse iterative covariance-based estimation (SPICE) [23] [24], likelihood-based estimation of sparse parameters (LIKES) [25], and sparse learning via iterative minimization (SLIM) [26]. We will demonstrate in this paper that the performance of ST-IAA is more powerful than these algorithms.

We choose to use the cascade imaging radar module [27] from TI as our experimental platform, which employs four AWR2243 chips cascaded together, consisting of a total of 12 transmit and 16 receive antennas. Relevant series of multi-chip and single-chip radar sensors from TI have been applied in various research studies [28]–[31]. The AWR2243 chip's capability for binary phase modulation per chirp allows us to implement ST-CDM with slow-time random binary codes on this experimental platform. Furthermore, for experimental convenience, we select 3 transmit and 4 receive antennas from the imaging radar board, constructing a 3×4 SLA design that is suitable for a single-chip radar sensor. Appendix A provides a detailed description of the antenna selection process. This leads to the creation of an ST-CDM MIMO radar prototype with a 3×4 SLA. Numerical and experimental verifications of the ST-IAA algorithm are conducted based on this radar prototype. The results indicate that ST-IAA significantly improves the imaging quality of the ST-CDM MIMO radar prototype with the 3×4 SLA design in comparison to conventional methods, for example, enabling the distinction of two adjacent cars traveling side by side at a distance of approximately 55 meters. Our contributions are summarized as follows.

1) We construct a single-chip ST-CDM radar prototype with a 3×4 SLA we designed.
2) We demonstrate that the robust ST-IAA algorithm can be used to suppress waveform separation residuals of ST-CDM and the angular sidelobe levels of SLAs.
3) The experiments indicate that the single-chip ST-CDM radar with the 3×4 SLA, when used with ST-IAA, can minimize the occurrence of velocity ambiguity and achieve an angular resolution of about 2°.

TABLE I
ABBREVIATIONS AND EXPANSIONS

3-D	three-dimensional
ADC	analog-to-digital converter
BPF	band-pass filter
CPI	coherent processing interval
DDM	Doppler-division multiplexing
FFT	fast Fourier transform
LFMCW	linear frequency-modulated continuous-wave
IAA	iterative adaptive approach
IF	intermediate frequency
LIKES	likelihood-based estimation of sparse parameters
LO	local oscillator
LPF	low-pass filter
LVDS	low voltage differential signaling
MF	matched filtering
MIMO	multiple-input multiple-output
NRMSE	normalized root-mean-square error
PRI	pulse repetition interval
SLA	sparse linear array
SLIM	sparse learning via iterative minimization
SNR	signal-to-noise ratio
SPICE	sparse iterative covariance-based estimation
ST-CDM	slow-time code-division multiplexing
ST-IAA	slow-time iteration adaptive approach
TDM	time-division multiplexing
TI	Texas Instruments
ULA	uniform linear array

The remainder of this paper is organized as follows. Section II establishes a signal model for the ST-CDM MIMO radar with M transmit and N receive antennas. In Section III, we introduce the ST-IAA algorithm and provide a complete data processing flow. Section IV provides numerical examples based on the parameters and arrays of our radar prototype to validate the imaging performance of ST-IAA. In Section V, we conduct a series of experiments using the radar prototype to evaluate the practical performance of using ST-IAA on the ST-CDM MIMO radar with SLAs. Section VI serves as the conclusion. Appendix A provides the antenna positions of the 3×4 SLA used in our radar prototype. All abbreviations used in this paper are summarized in Table I.

Notation: We use bold lowercase letters to denote vectors and bold uppercase letters to denote matrices. $(\cdot)^{\mathrm{T}}$ and $(\cdot)^{\mathrm{H}}$ denote the transpose and conjugate transpose of a vector or matrix, respectively. $(\cdot)^{-1}$ stands for the inverse of the

matrix. The superscript of a scalar $(\cdot)^*$ denotes the complex conjugate operation. $|\cdot|$ represents the element-wise modulus. $\|\cdot\|$ denotes the l_2-norm. We use $\mathbb{C}^{I_1\times I_2\times\cdots\times I_N}$ to represent the set of all complex-valued tensors of order N. The elements of $\mathcal{D}\in\mathbb{C}^{I_1\times I_2\times\cdots\times I_N}$ is denoted by $d_{i_1 i_2\cdots i_N}$. This paper utilizes tensors up to order 3. The tensors of order 1 and order 2 are commonly referred to as vectors and matrices, respectively. $\odot$ and $\otimes$ represent the Hadamard product and the Kronecker product, respectively.

II. Signal Model of ST-CDM MIMO Radar

Fig. 2(a) shows the diagram of a typical ST-CDM LFMCW MIMO radar system consisting of M transmit channels and N receive channels. For ease of presentation, this diagram depicts the scenario of a single-chip radar with $M = 3$ and $N = 4$. The LFMCW waveform and dechirp processing at each receive channel are illustrated in Fig. 2(b). The signal transmission process of the radar system from the transmit channels to the receive channels is described below and the signal model is provided as well.

A. Transmit Channels

The TI radar transceiver chip is able to store the complex envelopes of all transmitted chirps. In this paper, all chirps are assumed to possess the same complex envelope, which is given by

$$A_{\mathrm{c}}(t)=e^{j\pi\beta t^2}\,\mathrm{rect}\left(\frac{t-T_{\mathrm{c}}/2}{T_{\mathrm{c}}}\right), \tag{1}$$

where β is the slope of the rising portion of the chirp, T_{c} is the duration of the rising portion and $\mathrm{rect}(t)$ is the normalized rectangular function which is 1 if $-0.5\le t\le 0.5$ and 0 otherwise. The CPI is assumed to contain P chirps, or in other words, P slow-time samples. The ST-CDM MIMO radar uses M transmit channels to simultaneously transmit the chirps multiplied with different phase codes over slow-time. Let c_{mp} denote the random binary code adopted by the m-th transmit channel at the p-th chirp. Then the transmitted baseband signal of the m-th transmit channel in a CPI can be represented as

$$A_m(t)=\sum_{p=1}^{P}A_{mp}(t)=\sum_{p=1}^{P}c_{mp}A_{\mathrm{c}}\left[t-(p-1)T_{\mathrm{PRI}}\right]. \tag{2}$$

To be radiated to the space, the baseband signals must be modulated onto a sinusoidal carrier with frequency f_{c}. The emitted signal from the m-th transmit antenna is expressed as

$$s_m(t)=e^{j2\pi f_{\mathrm{c}}t}\sum_{p=1}^{P}c_{mp}A_{\mathrm{c}}\left[t-(p-1)T_{\mathrm{PRI}}\right]. \tag{3}$$

B. Receive Channels

The emitted signals are reflected after hitting the targets and their time delayed replicas are captured by the receive channels. The time delay of the propagation from the m-th transmit antenna to a target and then to the n-th receive antenna is given by

$$\tau_{mn}(t)=\frac{2(r+vt)}{c}+(x_m+y_n)\frac{\sin(\theta)}{c}, \tag{4}$$

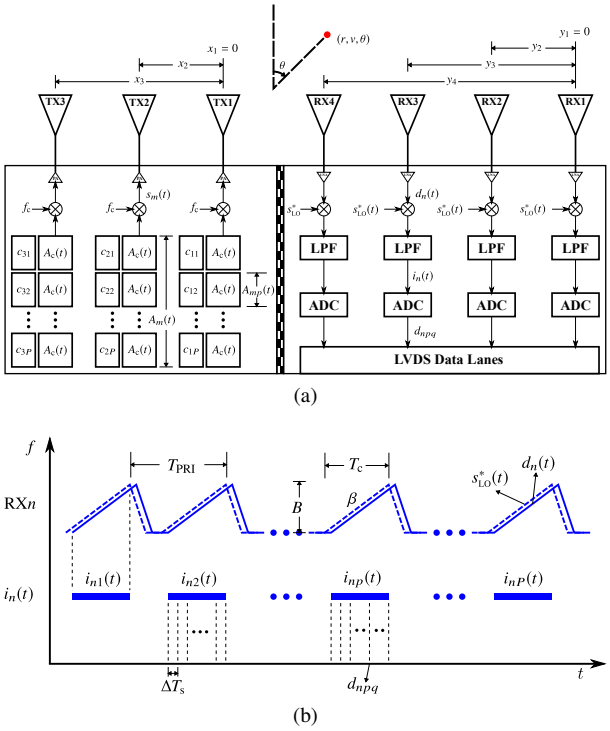

Fig. 2. (a) The diagram of a ST-CDM LFMCW MIMO radar with 3 transmit and 4 receive antennas. (b) Illustrations of the signal of local oscillator (LO), the signal of the n-th receiver, the IF signal and the captured raw data.

where c is the speed of light; (r, v, θ) are the range, radial velocity and angle of the target, respectively. x_m is the position of the m-th transmit antenna relative to the first one. Likewise, y_n is the position of the n-th receive antenna relative to the first one. That is to say, $x_1 = 0$ and $y_1 = 0$. And the spacing between these antennas can be non-uniform. Then, as shown by the solid zigzag line in Fig. 2(b), the received signal by the n-th receiver is

$$\begin{aligned}d_n(t)&=\eta\sum_{m=1}^{M}s_m\left[t-\tau_{mn}(t)\right]\\&=\eta\sum_{m=1}^{M}e^{j2\pi f_{\mathrm{c}}\left[t-\tau_{mn}(t)\right]}\sum_{p=1}^{P}c_{mp}\\&\quad\times A_{\mathrm{c}}\left[t-\tau_{mn}(t)-(p-1)T_{\mathrm{PRI}}\right],\end{aligned} \tag{5}$$

where η is the reflection coefficient of the target. We assume that $2r/c \gg 2vt/c + (x_m + y_n)\sin(\theta)/c$. Define $\tau_0 \triangleq 2r/c$. Then $d_n(t)$ can be approximated by:

$$\begin{aligned}d_n(t)\approx\eta\sum_{m=1}^{M}e^{j2\pi f_{\mathrm{c}}\left[t-\tau_{mn}(t)\right]}\sum_{p=1}^{P}c_{mp}\\\times A_{\mathrm{c}}\left[t-\tau_0-(p-1)T_{\mathrm{PRI}}\right].\end{aligned} \tag{6}$$

Subsequently, the received signals need to be demodulated with the signal of a local oscillator (LO), as shown by the dashed zigzag line in Fig. 2(b). The expression of the LO signal is shown as follows

$$s_{\mathrm{LO}}(t)=e^{j2\pi f_{\mathrm{c}}t}\sum_{p=1}^{P}A_{\mathrm{c}}\left[t-(p-1)T_{\mathrm{PRI}}\right]. \tag{7}$$

The mixed signal of $d_n(t)$ and $s_{\mathrm{LO}}(t)$, which is represented as $d_n(t)\, s_{\mathrm{LO}}^*(t)$, mainly contains two frequency components, namely high frequency and intermediate frequency (IF) ones, of which the latter carries useful information about the target. Subsequently the mixed signal passes through the low-pass filter (LPF) on each receiver and the output IF signal is expressed as

$$\begin{aligned} i_n(t) = \eta \sum_{m=1}^{M} e^{-j2\pi f_{\mathrm{c}} \tau_{mn}(t)} \sum_{p=1}^{P} c_{mp} \\ \times e^{j\pi\beta\tau_0^2} e^{-j2\pi\beta\tau_0[t-(p-1)T_{\mathrm{PRI}}]} \\ \times \mathrm{rect}\left[\frac{t-(p-1)\,T_{\mathrm{PRI}}-T_{\mathrm{c}}/2}{T_{\mathrm{c}}}\right], \end{aligned} \tag{8}$$

As shown by the thick solid lines in Fig. 2(b), the IF signal $i_n(t)$ is divided by rect() function into P partitions, one of which can be written as

$$\begin{aligned} i_{np}(t) = \eta \sum_{m=1}^{M} c_{mp} e^{-j2\pi\left[\frac{2r}{\lambda}+\frac{2vt}{\lambda}+(x_m+y_n)\frac{\sin(\theta)}{\lambda}\right]} \\ \times e^{j\pi\beta\tau_0^2} e^{-j2\pi\beta\tau_0[t-(p-1)T_{\mathrm{PRI}}]}, \\ (p-1)\,T_{\mathrm{PRI}} \le t \le T_{\mathrm{c}} + (p-1)\,T_{\mathrm{PRI}}, \end{aligned} \tag{9}$$

where $\lambda = c/f_{\mathrm{c}}$ is the wavelength. Since $\tau_0^2 \ll \tau_0 = 2r/c \ll 1$, this partition of the IF signal can be approximated as

$$\begin{aligned} i_{np}(t) \approx \eta' e^{-j2\pi y_n \frac{\sin(\theta)}{\lambda}} e^{-j2\pi\beta\tau_0[t-(p-1)T_{\mathrm{PRI}}]} \\ \times \sum_{m=1}^{M} c_{mp} e^{-j2\pi x_m \frac{\sin(\theta)}{\lambda}} e^{-j2\pi\frac{2vt}{\lambda}}, \end{aligned} \tag{10}$$

where $\eta' = \eta e^{-j2\pi\frac{2r}{\lambda}}$ can be regarded as the complex-valued amplitude of the target. The IF signal $i_{np}(t)$ is sampled by the analog-to-digital converter (ADC) at each receiver and converted to the captured raw data d_{npq}, $q = 1, \cdots, Q$, with Q denoting the fast-time sample number corresponding to each transmitted chirp, $p = 1, \cdots, P$, with P denoting the slow-time sample number (i.e., the number of chirps within a CPI), and $n = 1, \cdots, N$, with N denoting the receive antenna number. Let $t = (p-1)\,T_{\mathrm{PRI}} + (q-1)\,\Delta T_{\mathrm{s}}$, in which ΔT_{s} is the sampling interval for the ADC. Then

$$\begin{aligned} d_{npq} &= i_{np}\left[(p-1)\,T_{\mathrm{PRI}} + (q-1)\,\Delta T_{\mathrm{s}}\right] \\ &= \eta' e^{-j2\pi y_n \frac{\sin(\theta)}{\lambda}} e^{-j2\pi\beta\tau_0(q-1)\Delta T_{\mathrm{s}}} \\ &\quad \times \sum_{m=1}^{M} c_{mp} e^{-j2\pi x_m \frac{\sin(\theta)}{\lambda}} e^{-j2\pi\frac{2v}{\lambda}(p-1)T_{\mathrm{PRI}}} \\ &\quad \times e^{-j2\pi\frac{2v}{\lambda}(q-1)\Delta T_{\mathrm{s}}}. \end{aligned} \tag{11}$$

Note that $v\Delta T_{\mathrm{s}}/\lambda \ll 1$. So $e^{-j2\pi\frac{2v}{\lambda}(q-1)\Delta T_{\mathrm{s}}}$ is approximately constant within each chirp period. For notational simplicity, we denote $\eta' e^{-j2\pi\frac{2v}{\lambda}(q-1)\Delta T_{\mathrm{s}}}$ as α. Then (11) can be approximated as follows

$$\begin{aligned} d_{npq} \approx \alpha e^{-j2\pi y_n \frac{\sin(\theta)}{\lambda}} e^{-j2\pi\beta\tau_0(q-1)\Delta T_{\mathrm{s}}} \\ \times \sum_{m=1}^{M} c_{mp} e^{-j2\pi x_m \frac{\sin(\theta)}{\lambda}} e^{-j2\pi\frac{2v}{\lambda}(p-1)T_{\mathrm{PRI}}}, \end{aligned} \tag{12}$$

which describes a certain sampling point of the raw data captured by the ST-CDM transmission scheme. Note that (12) represents the echo signal of a single point target, whereas the actual raw data contains the superposition of signals reflected from multiple targets. When there are totally K point targets in the range-Doppler-angle region of interest, the three-dimensional (3-D) data model in the presence of additive noise can be expressed as

$$\begin{aligned} \bar{d}_{npq} \approx \sum_{k=1}^{K} \alpha_k e^{-j2\pi y_n \frac{\sin(\theta_k)}{\lambda}} e^{-j2\pi\beta\frac{2r_k}{c}(q-1)\Delta T_{\mathrm{s}}} \\ \times \sum_{m=1}^{M} c_{mp} e^{-j2\pi x_m \frac{\sin(\theta_k)}{\lambda}} e^{-j2\pi\frac{2v_k}{\lambda}(p-1)T_{\mathrm{PRI}}} \\ + \gamma_{npq}, \end{aligned} \tag{13}$$

where γ_{npq} denotes the white Gaussian noise. The data set $\left[\bar{d}_{npq}\right]$ is a tensor of order 3 denoted by $\mathcal{D}$. A data transmission technology called low-voltage differential signaling (LVDS) is used to export such 3-D raw data to a host computer. The noisy measurement tensor $\mathcal{D}$ can be used for the 3-D range-Doppler-angle imaging.

TABLE II
THE ST-IAA ALGORITHM

Input	$\boldsymbol{b}_{k_{\mathrm{r}}} = \left[b_{11k_{\mathrm{r}}}, \cdots, b_{1Pk_{\mathrm{r}}}, \cdots, b_{N1k_{\mathrm{r}}}, \cdots, b_{NPk_{\mathrm{r}}}\right]^{\mathrm{T}}$
	$\boldsymbol{A} = \left[\boldsymbol{a}\left(\tilde{\theta}_1, \tilde{v}_1\right), \cdots, \boldsymbol{a}\left(\tilde{\theta}_1, \tilde{v}_{K_{\mathrm{v}}}\right), \cdots, \boldsymbol{a}\left(\tilde{\theta}_{K_\theta}, \tilde{v}_1\right), \cdots, \boldsymbol{a}\left(\tilde{\theta}_{K_\theta}, \tilde{v}_{K_{\mathrm{v}}}\right)\right]$
Initiation	**create** $\boldsymbol{s}_{k_{\mathrm{r}}} = \frac{1}{N}\boldsymbol{A}^{\mathrm{H}}\boldsymbol{b}_{k_{\mathrm{r}}}$
	create $\boldsymbol{p} = \left[p_{11}, \cdots, p_{1K_{\mathrm{v}}}, \cdots, p_{K_\theta 1}, \cdots, p_{K_\theta K_{\mathrm{v}}}\right]^{\mathrm{T}}$
	where $p_{k_\theta k_{\mathrm{v}}} = \left\lvert s_{k_\theta k_{\mathrm{v}} k_{\mathrm{r}}}\right\rvert^2$
Iteration	**repeat**
	$\boldsymbol{R} = \boldsymbol{A}\mathrm{diag}\{\boldsymbol{p}\}\boldsymbol{A}^{\mathrm{H}}$
	for $k_\theta = 1, 2, \cdots, K_\theta$
	for $k_{\mathrm{v}} = 1, 2, \cdots, K_{\mathrm{v}}$
	$s_{k_\theta k_{\mathrm{v}} k_{\mathrm{r}}} = \frac{\boldsymbol{a}^{\mathrm{H}}\left(\tilde{\theta}_{k_\theta}, \tilde{v}_{k_{\mathrm{v}}}\right)\boldsymbol{R}^{-1}\boldsymbol{b}_{k_{\mathrm{r}}}}{\boldsymbol{a}^{\mathrm{H}}\left(\tilde{\theta}_{k_\theta}, \tilde{v}_{k_{\mathrm{v}}}\right)\boldsymbol{R}^{-1}\boldsymbol{a}\left(\tilde{\theta}_{k_\theta}, \tilde{v}_{k_{\mathrm{v}}}\right)}$
	$p_{k_\theta k_{\mathrm{v}}} = \left\lvert s_{k_\theta k_{\mathrm{v}} k_{\mathrm{r}}}\right\rvert^2$
	end
	end
	until convergence
Output	$\boldsymbol{s}_{k_{\mathrm{r}}} = \left[s_{11k_{\mathrm{r}}}, \cdots, s_{1K_{\mathrm{v}}k_{\mathrm{r}}}, \cdots, s_{K_\theta 1k_{\mathrm{r}}}, \cdots, s_{K_\theta K_{\mathrm{v}}k_{\mathrm{r}}}\right]^{\mathrm{T}}$
	$\boldsymbol{p} = \left[p_{11}, \cdots, p_{1K_{\mathrm{v}}}, \cdots, p_{K_\theta 1}, \cdots, p_{K_\theta K_{\mathrm{v}}}\right]^{\mathrm{T}}$

III. Range-Doppler-Angle Imaging

As described by (12), for an ST-CDM MIMO radar, the signals from the M transmit channels are superimposed together at each receive channel due to the simultaneous waveform transmissions. It is no longer feasible to use the conventional MF for waveform separation. Also, some algorithms that rely on the sample covariance matrix, such as the well-known MUSIC algorithm [32] [33], cannot be used with just a single snapshot, especially since spatial smoothing is impossible for SLAs. In this section, we present the ST-IAA algorithm, which is an extended version of IAA [15]–[17], to simultaneously

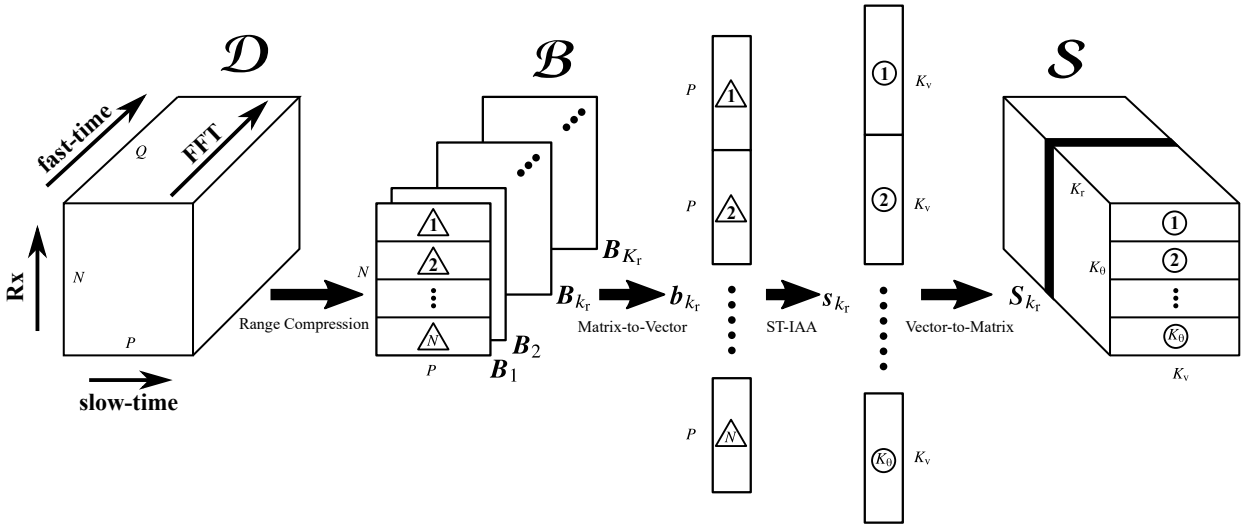

Fig. 3. Our proposed data processing flow in which the angle and velocity of targets are estimated by the ST-IAA algorithm.

address both the issue of high Doppler sidelobes arising from waveform separation residuals and the challenge of elevated angular sidelobes introduced by SLAs. ST-IAA can be used to generate Doppler-angle images with both high resolution and low sidelobes for the ST-CDM MIMO radar with SLAs.

After capturing data $\mathcal{D}$, to obtain the range profiles of targets with low computational complexities, we firstly perform range compression along the fast-time domain (i.e., within each chirp period) through windowed FFT. The range region of interest is discretized uniformly into K_{r} grids. Denote the result of range compression as $\mathcal{B}$ and one of its elements can be calculated as

$$b_{npk_{\mathrm{r}}} = \sum_{q=1}^{Q} w_q \bar{d}_{npq} e^{j2\pi\beta\frac{2\tilde{r}_{k_{\mathrm{r}}}}{c}(q-1)\Delta T_{\mathrm{s}}},\ k_{\mathrm{r}} = 1, \cdots, K_{\mathrm{r}}, \quad (14)$$

where $\{w_q\}_{q=1}^{Q}$ denote the window function used for range compression to reduce the sidelobe levels in the range dimension and $\{\tilde{r}_{k_{\mathrm{r}}}\}_{k_{\mathrm{r}}=1}^{K_{\mathrm{r}}}$ represent the range bins. After that, the range-Doppler-angle imaging problem can be simplified to the Doppler-angle imaging problem for each range bin.

We assume that there are K' targets, which is less than or equal to K in (13), at a given range bin k_r. Then (14) can be written as

$$b_{npk_{\mathrm{r}}} \approx \sum_{k=1}^{K'} \alpha'_k e^{-j2\pi y_n \frac{\sin(\theta_k)}{\lambda}} \sum_{m=1}^{M} c_{mp} e^{-j2\pi x_m \frac{\sin(\theta_k)}{\lambda}} \times e^{-j2\pi\frac{2v_k}{\lambda}(p-1)T_{\mathrm{PRI}}} + \gamma_{npk_{\mathrm{r}}}, \quad (15)$$

where α'_k represents the complex-valued amplitude of the k-th target in the slow-time and angular domain. Denote the k_{r}-th cross section of $\mathcal{B}$ as $\boldsymbol{B}_{k_{\mathrm{r}}}$, which is an $N \times P$ matrix. Note that all those elements $b_{npk_{\mathrm{r}}}$, where $n = 1, \cdots, N$ and $p = 1, \cdots, P$, are used to make up $\boldsymbol{B}_{k_{\mathrm{r}}}$, which can be expressed compactly as follows

$$\boldsymbol{B}_{k_{\mathrm{r}}} = \sum_{k=1}^{K'} \alpha'_k \boldsymbol{a}_{\mathrm{R}}(\theta_k) \left\{ \left[\boldsymbol{C}^{\mathrm{T}} \boldsymbol{a}_{\mathrm{T}}(\theta_k) \right] \odot \boldsymbol{a}_{\mathrm{D}}(v_k) \right\}^{\mathrm{T}} + \boldsymbol{\Gamma}_{k_{\mathrm{r}}}, \quad (16)$$

where $\boldsymbol{C}$ is an $M \times P$ slow-time coding matrix whose (m, p)-th element is c_{mp}; $\boldsymbol{\Gamma}_{k_{\mathrm{r}}}$ denotes the additive noise matrix; $\boldsymbol{a}_{\mathrm{T}}(\theta)$, $\boldsymbol{a}_{\mathrm{R}}(\theta)$ and $\boldsymbol{a}_{\mathrm{D}}(v)$, respectively, denote the transmit, receive and nominal temporal steering vectors with the following expressions

$$\boldsymbol{a}_{\mathrm{T}}(\theta) = \left[1, \cdots, e^{-j2\pi x_M \sin(\theta)/\lambda}\right]^{\mathrm{T}} \in \mathbb{C}^M, \quad (17)$$

$$\boldsymbol{a}_{\mathrm{R}}(\theta) = \left[1, \cdots, e^{-j2\pi y_N \sin(\theta)/\lambda}\right]^{\mathrm{T}} \in \mathbb{C}^N, \quad (18)$$

and

$$\boldsymbol{a}_{\mathrm{D}}(v) = \left[1, \cdots, e^{-j4\pi v(P-1)T_{\mathrm{PRI}}/\lambda}\right]^{\mathrm{T}} \in \mathbb{C}^P. \quad (19)$$

We intend to obtain the 2D Doppler-angle image $\boldsymbol{S}_{k_{\mathrm{r}}}$ at a given range bin k_{r} from $\boldsymbol{B}_{k_{\mathrm{r}}}$. Discretize the Doppler-angle region of interest into $K_\theta \times K_{\mathrm{v}}$ grid points uniformly, which are represented as $\{\tilde{\theta}_{k_\theta}\}_{k_\theta=1}^{K_\theta}$ and $\{\tilde{v}_{k_{\mathrm{v}}}\}_{k_{\mathrm{v}}=1}^{K_{\mathrm{v}}}$. Ensure $K_\theta \gg M \times N$ and $K_{\mathrm{v}} \gg P$, usually 5-10 times larger, so that the mesh grids are fine enough. We have $\boldsymbol{S}_{k_{\mathrm{r}}} \in \mathbb{C}^{K_\theta \times K_{\mathrm{v}}}$. Then we can formulate (16), at least approximately, using the following linear model

$$\boldsymbol{b}_{k_{\mathrm{r}}} = \boldsymbol{A}\boldsymbol{s}_{k_{\mathrm{r}}} + \boldsymbol{\gamma}_{k_{\mathrm{r}}}, \quad (20)$$

where $\boldsymbol{b}_{k_{\mathrm{r}}}$, $\boldsymbol{s}_{k_{\mathrm{r}}}$ and $\boldsymbol{\gamma}_{k_{\mathrm{r}}}$ are the vectorizations of $\boldsymbol{B}_{k_{\mathrm{r}}}$, $\boldsymbol{S}_{k_{\mathrm{r}}}$ and $\boldsymbol{\Gamma}_{k_{\mathrm{r}}}$, respectively. And the steering matrix $\boldsymbol{A}$ can be written as

$$\boldsymbol{A} = \left[\boldsymbol{a}\left(\tilde{\theta}_1, \tilde{v}_1\right), \cdots, \boldsymbol{a}\left(\tilde{\theta}_1, \tilde{v}_{K_{\mathrm{v}}}\right), \cdots, \boldsymbol{a}\left(\tilde{\theta}_{K_\theta}, \tilde{v}_1\right), \cdots, \boldsymbol{a}\left(\tilde{\theta}_{K_\theta}, \tilde{v}_{K_{\mathrm{v}}}\right)\right], \quad (21)$$

where $\boldsymbol{a}(\theta, v)$ is expressed as

$$\boldsymbol{a}\left(\tilde{\theta}_{k_\theta}, \tilde{v}_{k_{\mathrm{v}}}\right) = \boldsymbol{a}_{\mathbf{R}}\left(\tilde{\theta}_{k_\theta}\right) \otimes \left\{ \left[\boldsymbol{C}^{\mathrm{T}} \boldsymbol{a}_{\mathbf{T}}\left(\tilde{\theta}_{k_\theta}\right) \right] \odot \boldsymbol{a}_{\mathbf{D}}\left(\tilde{v}_{k_{\mathrm{v}}}\right) \right\}. \quad (22)$$

The ST-IAA algorithm can be used to estimate $\boldsymbol{s}_{k_{\mathrm{r}}}$ from the noisy measurements $\boldsymbol{b}_{k_{\mathrm{r}}}$. The algorithm flow of ST-IAA is summarized in Table II. The ST-IAA algorithm initializes $\boldsymbol{s}_{k_{\mathrm{r}}}$ and the power vector $\boldsymbol{p}$ using the conventional MF method at the beginning. Then, ST-IAA iteratively updates $\boldsymbol{s}_{k_{\mathrm{r}}}$ and $\boldsymbol{p}$. During each iteration, the ST-IAA covariance matrix $\boldsymbol{R}$ is calculated

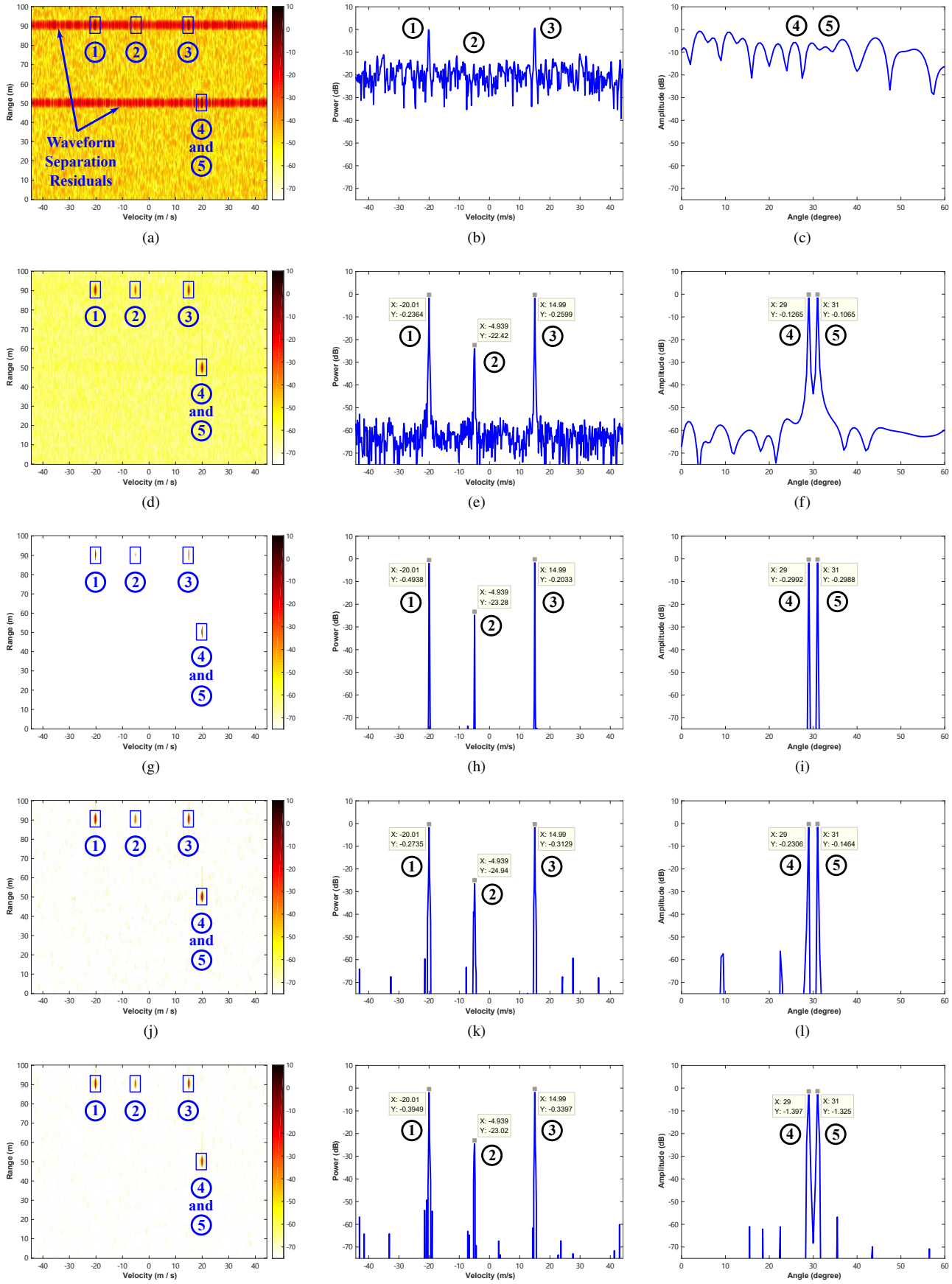

Fig. 4. Imaging results of the five targets: (a)(b)(c) The conventional MF; (d)(e)(f) The ST-IAA algorithm; (g)(h)(i) SLIM; (j)(k)(l) LIKES; (m)(n)(o) SPICE.

with the diagonalization of $\boldsymbol{p}$, which forms a diagonal matrix with $\boldsymbol{p}$ on the diagonal, i.e.,

$$\boldsymbol{R} = \boldsymbol{A}\mathrm{diag}\{\boldsymbol{p}\}\boldsymbol{A}^{\mathrm{H}}. \tag{23}$$

Then the formula below is used to update $\boldsymbol{s}_{k_\mathrm{r}}$,

$$s_{k_\theta k_\mathrm{v} k_\mathrm{r}} = \frac{\boldsymbol{a}^{\mathrm{H}}\left(\tilde{\theta}_{k_\theta}, \tilde{v}_{k_\mathrm{v}}\right)\boldsymbol{R}^{-1}\boldsymbol{b}_{k_\mathrm{r}}}{\boldsymbol{a}^{\mathrm{H}}\left(\tilde{\theta}_{k_\theta}, \tilde{v}_{k_\mathrm{v}}\right)\boldsymbol{R}^{-1}\boldsymbol{a}\left(\tilde{\theta}_{k_\theta}, \tilde{v}_{k_\mathrm{v}}\right)}. \tag{24}$$

Note that if $\boldsymbol{R}$ is equal to the identity matrix $\boldsymbol{I}$, (24) becomes the conventional MF method. Also, ST-IAA does not require the prior knowledge about the target number K' since it is a nonparametric approach. Through the iterations described in Table II, we can generate the high-resolution Doppler-angle image $\boldsymbol{S}_{k_\mathrm{r}}$ from $\boldsymbol{B}_{k_\mathrm{r}}$ with both the problems of waveform separation residuals and high angular sidelobes of SLAs mitigated. The processing flow of the captured raw data $\mathcal{D}$ is summarized in Fig. 3. Once the Doppler-angle images are generated for all range bins, we finally obtain the 3-D range-Doppler-angle image $\mathcal{S}$ containing the information about the range, radial velocity and angle of all targets.

IV. Numerical Examples

In this section, we evaluate the performance of the ST-IAA algorithm using numerical examples. For the ST-CDM MIMO radar with SLAs, this evaluation primarily comprises two aspects. On the one hand, this involves confirming whether ST-IAA can be used to effectively suppress the Doppler sidelobes caused by waveform separation residuals. On the other hand, it aims to verify whether ST-IAA can be used to reduce the angular sidelobe levels of SLAs while taking full advantage of their high angular resolution capabilities.

To achieve goals above in simulations, we set up five ideal point targets with different parameters, as listed in Table III. Among them, the first three targets have different velocities and intensities, while the last two targets have an angular difference of 2°. In addition, we simulate an ST-CDM LFMCW MIMO radar system with $M = 3$ transmit antennas and $N = 4$ receive antennas. The antenna arrangement follows the position vectors of the 3×4 SLA given in (42) of Appendix A. All transmit channels emit chirps synchronously, the number of which in a CPI is $P = 384$. Therefore, the size of the slow-time random binary code matrix $\boldsymbol{C}$ is 3×384. The ADC component of each receive channel extracts $Q = 128$ samples along the fast-time (i.e., each chirp period). As a result, the captured data for a single snapshot $\mathcal{D}$ has $4 \times 384 \times 128$ elements.

We also provide a set of practical waveform parameters for simulations. Specifically, the carrier frequency is $f_\mathrm{c} = 77\,\mathrm{GHz}$ and the PRI is $T_\mathrm{PRI} = 22\,\mu\mathrm{s}$. Then the maximum unambiguous detectable velocity is calculated as follows

$$v_{\max} = \frac{c}{4 f_\mathrm{c} T_\mathrm{PRI}} \approx 44.27\,\mathrm{m/s}. \tag{25}$$

In addition, the chirp slope is $\beta = 15\,\mathrm{MHz}/\mu\mathrm{s}$ and the sampling rate is $f_\mathrm{s} = 20\,\mathrm{MSPS}$. Considering the fact that the sampling rate is twice the bandwidth of the IF signal, we use the formula below to calculate the maximum detectable range

$$r_{\max} = \frac{f_\mathrm{s} c}{4\beta} = 100\,\mathrm{m}. \tag{26}$$

TABLE III
Parameters of Targets

k	①	②	③	④	⑤
Range (m)	90	90	90	50	50
Velocity (m/s)	−20	−5	15	20	20
Angle (deg)	−20	−20	−20	29	31
Intensity	1	0.1	1	1	1

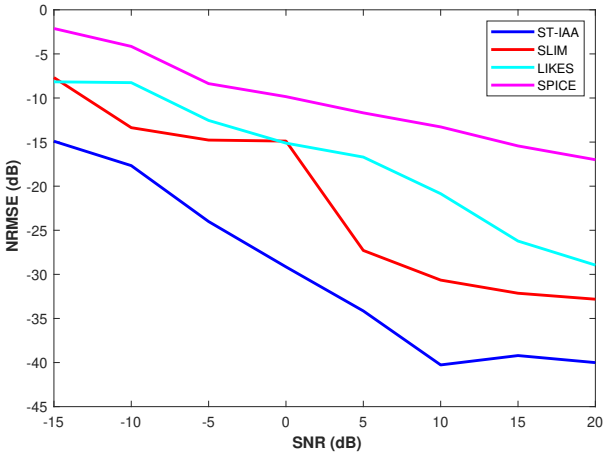

Fig. 5. The normalized root-mean-square errors (NRMSE) for the target intensities estimated by ST-IAA, SLIM, LIKES and SPICE.

TABLE IV
Iteration Number and Computation Time

	ST-IAA	**SLIM**	**LIKES**	**SPICE**
Iteration Number	7	7	15	30
Computation Time (s)	66.1	25.7	145.2	268.6

We first present the imaging result of the conventional MF method to visually demonstrate the presence of waveform separation residuals, as shown in Figs. 4(a)–(c). The process of waveform separation and imaging in the MF method is relatively straightforward. Specifically, let $\boldsymbol{c}_m$ represent the m-th row of the code matrix $\boldsymbol{C}$, i.e.,

$$\boldsymbol{C} = \left[\boldsymbol{c}_1^{\mathrm{T}}, \boldsymbol{c}_2^{\mathrm{T}}, \cdots, \boldsymbol{c}_m^{\mathrm{T}}, \cdots, \boldsymbol{c}_M^{\mathrm{T}}\right]^{\mathrm{T}}. \tag{27}$$

Then $\boldsymbol{B}_{k_\mathrm{r}}\mathrm{diag}\{\boldsymbol{c}_m\}$, $m = 1, \cdots, M$, is the separated signal corresponding to the transmitted signal from the m-th transmitter, as well as any residuals due to the other transmitted signals. Define $\mathcal{G}$ as the three-dimensional data stacking all of these M matrices. Similarly, let $\boldsymbol{G}_{k_\mathrm{r}}$ denote the k_r-th cross section of $\mathcal{G}$. The matrix $\boldsymbol{G}_{k_\mathrm{r}}$ can be denoted as

$$\boldsymbol{G}_{k_\mathrm{r}} = \left[\mathrm{diag}\{\boldsymbol{c}_1\}\boldsymbol{B}_{k_\mathrm{r}}^{\mathrm{T}}, \cdots, \mathrm{diag}\{\boldsymbol{c}_M\}\boldsymbol{B}_{k_\mathrm{r}}^{\mathrm{T}}\right]^{\mathrm{T}}, \tag{28}$$

from which we can see that $\boldsymbol{G}_{k_\mathrm{r}}$ has MN rows and P columns. Then, the MF method utilizes a straightforward FFT in the slow-time domain of $\mathcal{G}$ to obtain the range-Doppler image shown in Fig. 4(a). As depicted in Fig. 4(b), the target with the lowest intensity, i.e., the 2nd target, is masked by the high waveform separation residuals of the other stronger targets. Furthermore,

(a) (b)

Fig. 6. The minimum angle separation of two corner reflectors that can be resolved using different antenna arrangements on the ST-CDM radar prototype: (a) about 5.6° when using the 3×4 ULA; (b) about 2.8° when using the 3×4 SLA.

due to the sparse array on the radar, the nonuniform FFT [34] is employed to obtain the angular information of targets, as shown in Fig. 4(c). It can be observed that the conventional MF method is entirely unsuitable for the ST-CDM radar with SLAs.

(d)–(f) present the imaging results for the ST-IAA algorithm. As depicted in Fig. 4(e), in contrast to the conventional MF method, ST-IAA clearly reveals the 2nd target with the weakest intensity without encountering the issue of high Doppler sidelobes caused by waveform separation residuals. Also, as shown in Fig. 4(f), ST-IAA operates effectively on the sparse array and achieves superior angular resolution compared to the Rayleigh resolution of the 3×4 SLA in (42). Based on the steering matrix in (21) constructed for the ST-CDM signal model, we explore the application of several other well-known hyperparameter-free estimation algorithms, such as SPICE [23] [24], LIKES [25], and SLIM [26].

The imaging results of the ST-CDM radar with the 3×4 SLA using SLIM, LIKES, and SPICE are shown in Figs. 4(g)–(o). Like the ST-IAA algorithm, they can also effectively address the issues suffered by the conventional MF method, and obtain accurate estimates of target velocities and angles. However, the estimation accuracy for the target intensities vary considerably among these four algorithms. Fig. 5 shows the normalized root-mean-square errors (NRMSE) for their target intensity estimates under different signal-to-noise ratios (SNR). The formula used to calculate NRMSE is given by

$$\text{NRMSE} = \sqrt{\frac{1}{RK} \sum_{r=1}^{R} \sum_{k=1}^{K} \frac{\left| \hat{\alpha}_k^{(r)} - \alpha_k \right|^2}{\alpha_k^2}}, \tag{29}$$

where $\hat{\alpha}_k^{(r)}$ represents the intensity estimate of the k-th target obtained in the r-th Monte Carlo simulation. It is evident in Fig. 5 that ST-IAA demonstrates superior estimation accuracy compared to the other algorithms.

We also provide the number of iterations and the computation time required for convergence of these hyperparameter-free algorithms in Table IV. Under the ST-CDM signal model, ST-IAA and SLIM not only exhibit superior estimation accuracy compared to LIKES and SPICE, but also have much faster computation speed than the latter two. Furthermore, although ST-IAA is not as fast as SLIM in terms of computation speed, the former holds a significant advantage in estimation accuracy and robustness. The robustness advantage of ST-IAA in handling real ST-CDM radar data will be demonstrated in experiments of the next section.

V. Experimental Measurements and Imaging Results

The experiments consist of two parts, indoor stationary testing and outdoor road testing. The former is conducted by using corner reflectors as static targets to preliminarily evaluate the advantages of using SLAs on the ST-CDM radar and the robustness of the ST-IAA algorithm. The latter is a set of comparative experiments conducted on a provincial road, aiming to highlight the advantages of using ST-IAA for 3-D imaging with the ST-CDM radar equipped with the 3×4 SLA in practical applications. The experimental methodologies and imaging results for these two categories of tests are described in detail in the following two subsections.

A. Indoor Stationary Testing

We use two categories of antenna arrangements on our ST-CDM radar prototype: the 3×4 ULA given in (34) and the 3×4 SLA given in (42). Two corner reflectors are placed in front of the radar to ensure that they are equidistant from the radar. The angular difference between those two corner reflectors is determined by both the distance between them and their distance to the radar. Throughout the testing, we maintain a fixed radar position while gradually changing the positions of the corner reflectors. We start with a large angular separation and gradually decrease the angular difference between those two corner reflectors. As the ST-IAA algorithm can achieve super resolution, the 3×4 ULA can still be used to distinguish those two corner reflectors even when the angular difference is less than its Rayleigh angular resolution of 8.5°. We gradually decrease the angular difference, and those two peaks in the angular spectrum are almost merging together when the angular difference reaches to about 5.6°, as shown in Fig. 6(a) and the blue line in Fig. 7(g). This indicates that the 3×4 ULA can only distinguish two targets with a minimum angular difference of approximately 5.6° when using the ST-IAA algorithm.

Next we use the 3×4 SLA to repeat the testing. We further decrease the spacing between the two corner reflectors while

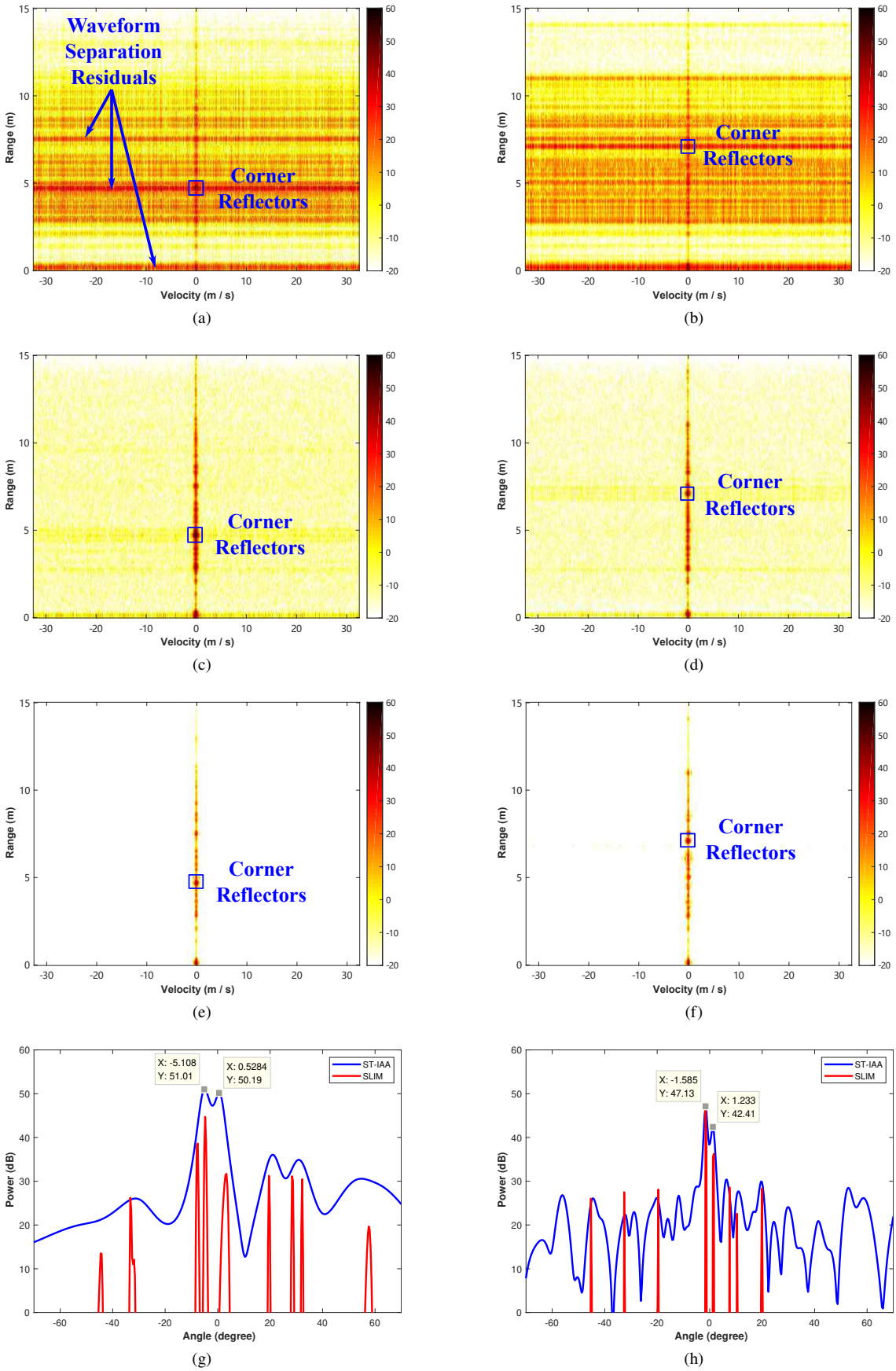

Fig. 7. The ST-CDM radar with the 3×4 ULA: (a) the imaging result of MF; (c) ST-IAA; (e) SLIM; (g) the angular spectra generated by ST-IAA and SLIM. The ST-CDM radar with the 3×4 SLA: (b) MF; (d) ST-IAA; (f) SLIM; (h) the angular spectra of ST-IAA and SLIM.

increasing the distance between the corner reflectors and the radar. Due to the space limitations of our indoor laboratory, the minimum angular difference between the two corner reflectors that can be achieved in our laboratory is approximately 2.8°. The 3×4 SLA can easily distinguish those two corner reflectors with the assistance of ST-IAA. The experimental scenario and the corresponding angular spectrum are illustrated in Fig. 6(b) and the blue line in Fig. 7(h). Moreover, although Fig. 13 indicates that the sidelobe level of the 3×4 SLA is much higher than that of the 3×4 ULA, ST-IAA can reduce the sidelobe level of the former's angular spectrum to be comparable to the latter. It can also be observed from Figs. 7(a)(b) and 7(c)(d) that ST-IAA can significantly suppress the Doppler sidelobes arising from the waveform separation residuals suffered by the conventional MF method.

In addition, to demonstrate the robustness of the ST-IAA algorithm, we present the imaging results of SLIM, which has lower estimation accuracy and shorter computation time compared to the former. As shown in Figs. 7(e)(f), like the ST-IAA algorithm, SLIM can also address the problem of waveform separation residuals. However, SLIM fails to provide high quality angular spectra for practical antenna arrays. As illustrated by the red lines in Figs. 7(g)(h), compared to ST-IAA, SLIM obviously lacks accuracy in estimating the angles and intensities of targets. In summary, ST-IAA stands out as the optimal choice for the ST-CDM radar imaging. The performance of the ST-CDM radar with the 3×4 SLA in a highly dynamic environment is demonstrated by the outdoor experiments discussed in the following subsection.

B. Outdoor Road Testing

The outdoor testing was carried out on a provincial road. The complex environments help highlight the advantages of the ST-CDM radar equipped with the SLA and the robustness of the ST-IAA algorithm. Fig. 8(a) shows the experimental setup, which includes three radars and one camera. As indicated by the red arrow in Fig. 8(b), the three radars are positioned at the junction of the road to observe the vehicles ahead concurrently. They are configured with different parameters listed in Table V for the sake of comparison. And the camera records videos for subsequent viewing and analysis.

First, let us discuss the common features of these three radars. The parameters of the 1st radar is similar to those of the simulated ST-CDM radar, i.e., $r_{\max} = 100\,\text{m}$. In addition, the range resolution is

$$r_{\text{res}} = \frac{c}{2\beta T_{\text{c}}} = 0.56\,\text{m}. \tag{30}$$

And the velocity resolution can be calculated as follows:

$$v_{\text{res}} = \frac{c/f_{\text{c}}}{2PT_{\text{PRI}}} = 0.23\,\text{m/s}. \tag{31}$$

According to the parameters provided by Table V along with the formulas (26), (30) and (31), $r_{\max}$, r_{res} and v_{res} are also the same for the other two radars to ensure the consistency of the basic performance.

There are two main differences among the three radars (see Table V). One is that the antenna arrays of the 3rd radar (ULAs)

(a) (b)

Fig. 8. (a) The three radars used in the outdoor experiments. (b) The illustration of the road junction and the placement of radars.

TABLE V
THE PARAMETERS OF THREE RADARS

Identifier	①	②	③
Scheme	ST-CDM	TDM	TDM
Array	3×4 SLA	3×4 SLA	3×4 ULA
f_{c} (GHz)	77	77	77
T_{c} (μs)	18	18	18
β (MHz/μs)	15	15	15
T_{PRI} (μs)	22	66	66
f_{s} (MSPS)	20	20	20
Q	128	128	128
P	384	128	128

are different from those of the 1st and 2nd radars (SLAs). And the other one is that the transmission schemes of the 1st radar (ST-CDM) is different from those of the 2nd and 3rd radars (TDM). For the former difference, we expect to show the advantages of SLAs over ULAs with the same number of antennas. For the latter difference, we intend to demonstrate that the ST-CDM transmission scheme can achieve greater maximum unambiguous detectable velocity than TDM with the same frame length (i.e., CPI). The frame length, as the name suggests, is the duration of a LFMCW frame, defined as PT_{PRI}. Note that using the same frame length ensures the same velocity resolution as described in (31). According to (25), the maximum unambiguous detectable velocity of the 1st radar is $v_{\max} = 44.27$ m/s, whereas that of the 2nd and 3rd radar is only $v_{\max} = \frac{44.27}{3}$ m/s = 14.76 m/s.

We first consider an experimental scenario in which two cars are approaching the radars from a distance at slightly different speeds, and there is a truck traveling in the same direction at a closer distance, as shown in Fig. 9(a). Figs. 9(b)(c) present the imaging results of the 1st radar using the ST-IAA algorithm. Although the two cars are very close to each other, they can be easily distinguished in the Doppler dimension due to the their speed difference and the high velocity resolution in (31). As a comparison between the unambiguous Doppler ranges of ST-CDM and TDM, the imaging results of the 2nd and 3rd radars are shown in Figs. 9(d)–(g). It can be observed that the radial velocity of car-2 slightly exceeds the unambiguous Doppler ranges of these two TDM radars, resulting in the detection of car-2's motion status as moving away. The 1st radar, i.e., the ST-CDM radar, with its much larger unambiguous Doppler

(a)

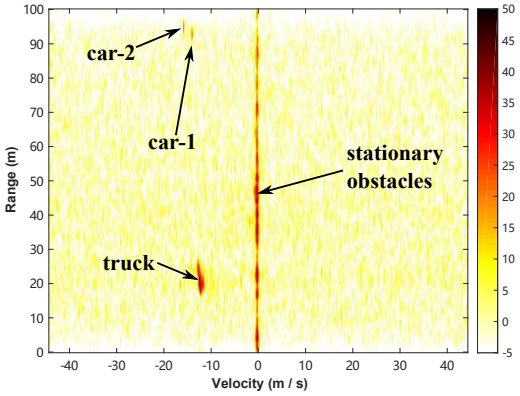

(b)

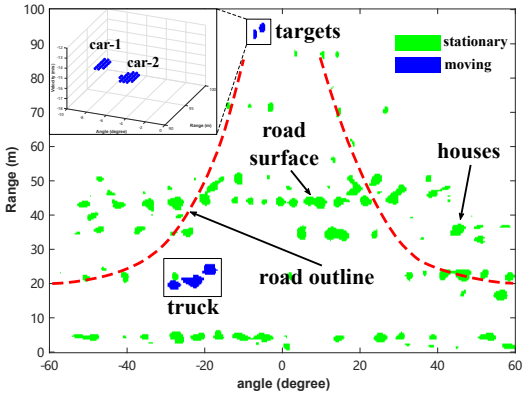

(c)

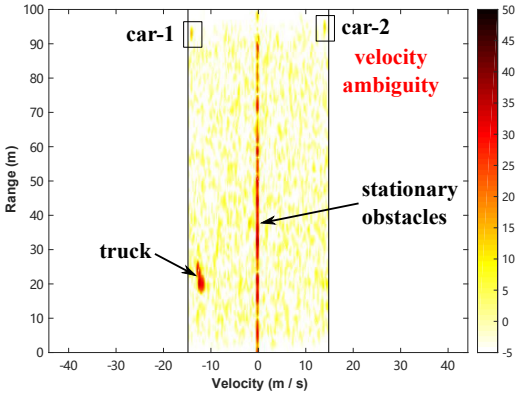

(d)

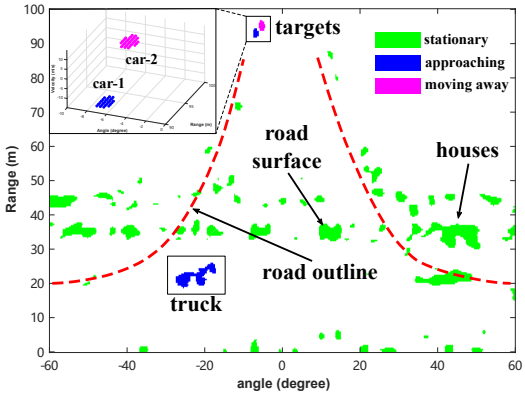

(e)

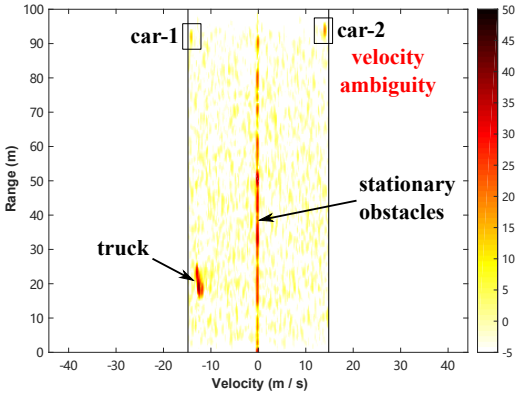

(f)

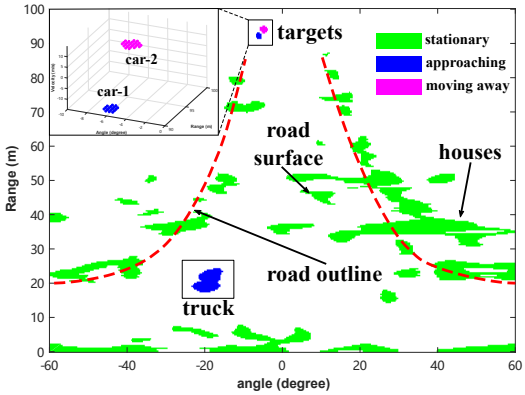

(g)

Fig. 9. (a) The first experimental scenario with a truck approaching at close distance and two cars traveling at slightly different speeds at a distance. (b)(c) The imaging results of the 1st radar; (d)(e) the 2nd radar; (f)(g) the 3rd radar.

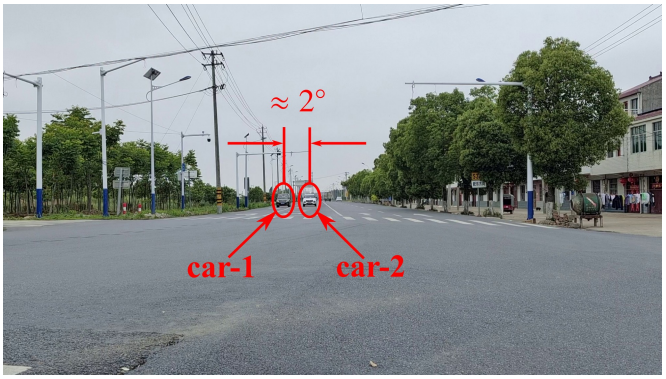

(a)

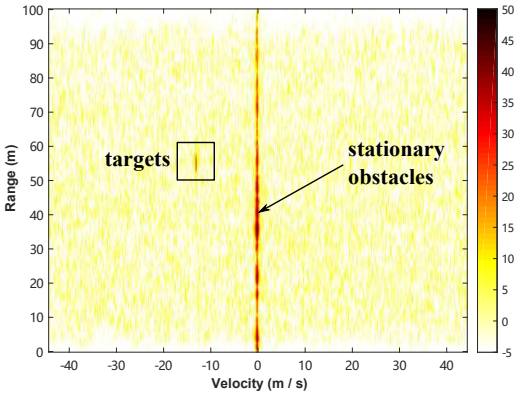

(b)

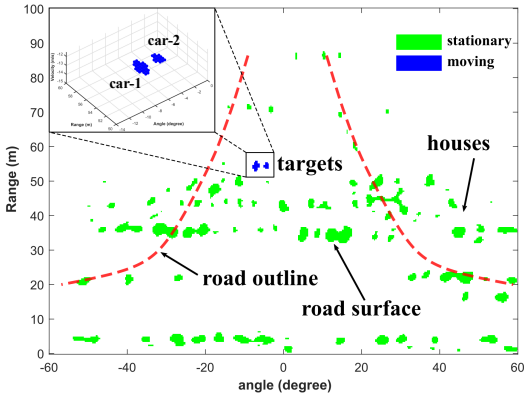

(c)

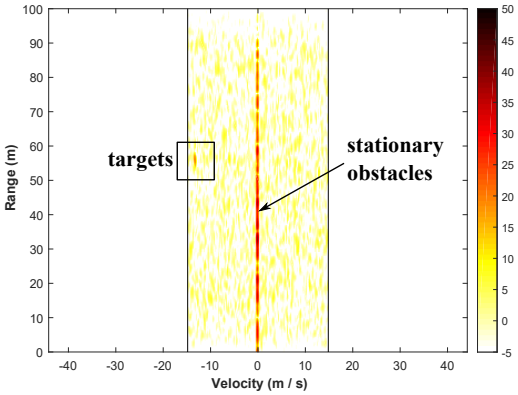

(d)

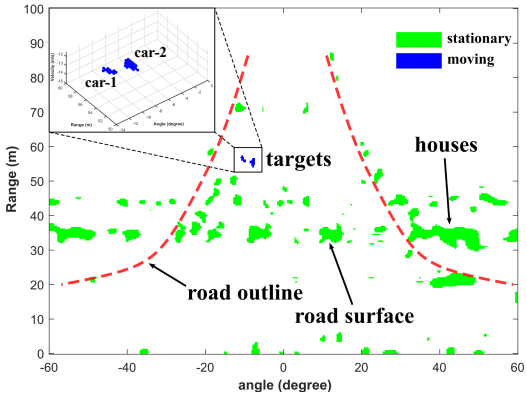

(e)

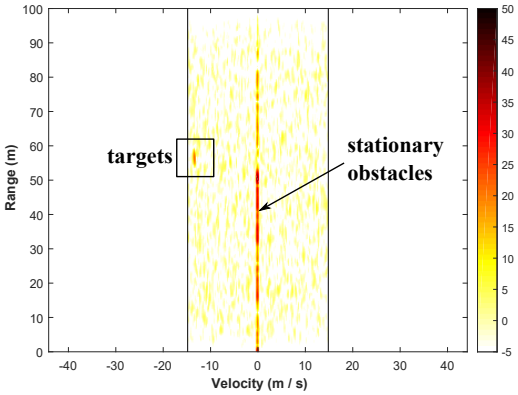

(f)

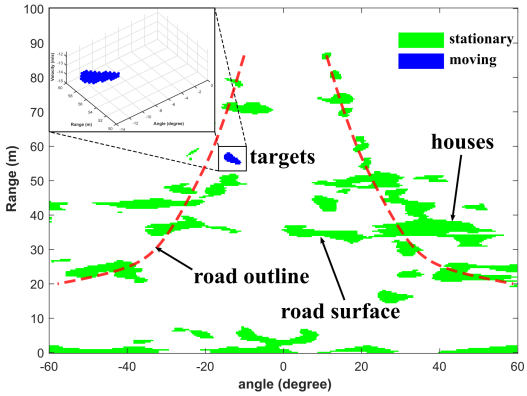

(g)

Fig. 10. (a) The second experimental scenario with two approaching cars side by side at the same speed. (b)(c) The imaging results of the 1st radar; (d)(e) the 2nd radar; (f)(g) the 3rd radar.

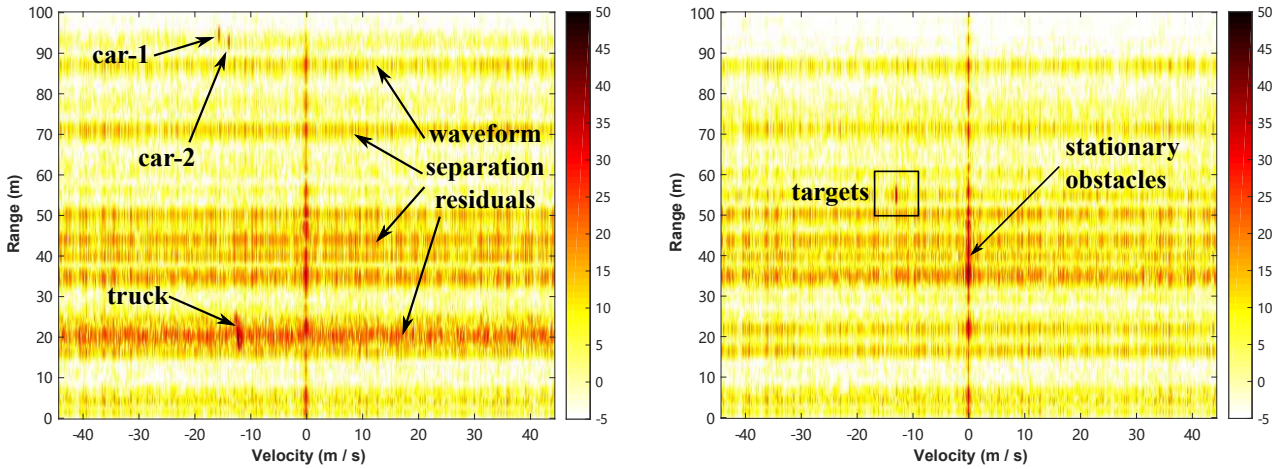

(a) (b)

Fig. 11. The range-Doppler images of the 1st radar generated by the conventional MF method: (a) the first scenario; (b) the second scenario.

range, can significantly reduce the probability of such errors, which is crucial for highly dynamic environments. From this, the advantage of the ST-CDM radar over its TDM counterpart is demonstrated.

The second scenario we consider is shown in Fig. 10(a), where two cars approach the radars side by side at the same speed of about 13 m/s and the same range of about 55 m while the distance between them is approximately 2 m. So, none of the three radars can distinguish these two cars in both the range and Doppler dimensions, as shown in Figs. 10(b)(d)(f). Considering the width of the cars, the angular difference arising from the transverse gap between those two cars is approximately 2°. With this condition, the 3rd radar with the 3×4 ULA has no capability to distinguish those two cars as shown in Fig. 10(g). In contrast, the 2nd radar with the 3×4 SLA is able to distinguish them as shown in Fig. 10(e). At the same time, as shown in Fig. 10(c), the 1st radar with the 3×4 SLA working in the ST-CDM mode can also distinguish them, which verifies the high performance and stability of our ST-IAA algorithm when using SLAs. It's noteworthy that this angular resolution of approximately 2° is achieved using only 3 transmit and 4 receive channels from a single AWR2243 chip, approaching the angular resolution of the TI four-chip cascaded radar [27].

We also use the conventional MF method to process the data from the 1st radar working in the ST-CDM mode, as shown in Figs. 11(a)(b). The presence of multiple horizontal ridges in the range-Doppler image is attributed to waveform separation residuals, which can reduce the dynamic range of the ST-CDM radar and negatively impact the detection of targets with weak reflections. In comparison, the corresponding imaging results of ST-IAA shown in Fig. 9(b) and Fig. 10(b) is free from those ridges so that all moving targets can be detected easily. Thus the excellent capability of the ST-IAA algorithm to suppress waveform separation residuals and angular sidelobes, leading to high quality radar imaging, is verified experimentally using the ST-CDM MIMO radar prototype equipped with the 3×4 SLA we designed.

VI. Conclusion

The ST-CDM MIMO radar has the advantages of concentrated energy radiation, absence of virtual array distortion, and large maximum unambiguous detectable velocity. We have shown that the ST-IAA algorithm can be used to mitigate the problem of waveform separation residuals in the ST-CDM radar, which hinders its widespread deployment. Moreover, using SLAs can significantly enhance the angular resolution of a single-chip ST-CDM MIMO radar sensor but suffers from high angular sidelobe problems. We have shown that ST-IAA can also be used to significantly reduce the high angular sidelobes of SLAs. We provide both numerical and experimental examples to showcase the outstanding performance of the ST-CDM MIMO radar with SLAs when using the ST-IAA algorithm. For the experiments, we construct an ST-CDM MIMO radar prototype with a 3×4 SLA we designed. The mechanisms of this prototype can be used to form a single-chip radar sensor with an angular resolution close to that of the TI four-chip cascaded radar. Through indoor stationary testing and outdoor road testing, the superior imaging performance of the ST-CDM MIMO radar equipped with the 3×4 SLA using the ST-IAA algorithm is demonstrated.

Appendix A
Sparse Linear Array Design

A typical single-chip radar sensor is equipped with only 3 transmit and 4 receive antennas, as discussed in Section I. Our goal is to design a 3×4 SLA to improve the angular resolution of a single-chip radar sensor. Fig. 12(a) shows the experimental platform, which is a multi-chip radar module. The relative positions of 12 transmit antennas and 16 receive antennas on the radar board are depicted in Fig. 12(b). With the MIMO framework, this 12×16 array can generate up to 192 virtual elements, including 134 non-overlapping virtual elements, as illustrated in Fig. 12(c). Among the numerous virtual elements, a total of 86 elements are arranged in a straight line with half-wavelength spacing, forming an aperture of 42.5λ, as depicted in the bottom row of Fig. 12(c). These uniformly spaced elements

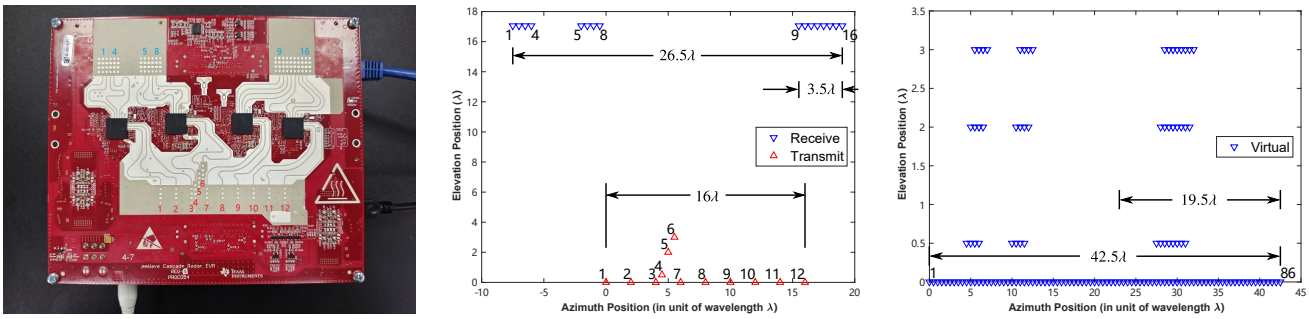

(a) (b) (c)

Fig. 12. (a) The TI cascade imaging radar module. (b) The relative positions of transmit and receive antennas. (c) The MIMO virtual array.

provide favorable conditions for us to select 12 elements to form a 3×4 SLA. The selected 3×4 SLA can be used by single-chip radar sensors.

First of all, we utilize the array steering vector to define the normalized beam pattern that characterizes array performance. The steering vectors of the transmit and receive arrays are already given by (17) and (18) in Section II. Then the steering vector of the virtual array can be written as

$$\begin{aligned}\boldsymbol{a}_{\mathrm{V}}(\theta) &= \left[1, \cdots, e^{-j2\pi z_L \sin(\theta)/\lambda}\right]^{\mathrm{T}} \\ &= \boldsymbol{a}_{\mathrm{T}}(\theta) \otimes \boldsymbol{a}_{\mathrm{R}}(\theta),\end{aligned} \tag{32}$$

where the position of the l-th virtual element is $z_l = x_m + y_n$. The number of virtual array elements is $L = M \times N$, which may include some overlapping elements. The normalized array beam pattern is defined as

$$\Phi(\theta) = \frac{\left|\boldsymbol{a}_{\mathrm{V}}^T(\theta)\,\boldsymbol{w}\right|}{\left\|\boldsymbol{a}_{\mathrm{V}}(\theta)\right\|^2} = \frac{1}{L}\left|\sum_{l=1}^{L} e^{-j2\pi z_l \sin(\theta)/\lambda}\right|, \tag{33}$$

where θ belongs to $[-90°, 90°]$, and the weight vector $\boldsymbol{w} = [1, 1, \cdots, 1]^T$, which means that the mainlobe of the normalized array beam pattern is oriented in the normal direction of the array, i.e., $\theta_0 = 0°$.

We take a typical 3×4 ULA as an example to visually illustrate the normalized beam pattern. The position vectors of the 3×4 ULA are given as

$$\boldsymbol{x} = [0,\ 2\lambda,\ 4\lambda], \tag{34a}$$

$$\boldsymbol{y} = [0,\ 0.5\lambda,\ 1\lambda,\ 1.5\lambda]. \tag{34b}$$

corresponding to the 1st, 2nd, and 3rd transmit antennas, as well as the 1st, 2nd, 3rd, and 4th receive antennas in Fig. 12(b). And the positions of virtual elements can be calculated as

$$\begin{aligned}\boldsymbol{z} = [&0,\ 0.5\lambda,\ 1\lambda,\ 1.5\lambda,\ 2\lambda,\ 2.5\lambda,\ 3\lambda,\\ &3.5\lambda,\ 4\lambda,\ 4.5\lambda,\ 5\lambda,\ 5.5\lambda].\end{aligned} \tag{35}$$

These 12 uniformly spaced elements, each separated by one half of a wavelength, correspond to the first 12 virtual elements in the bottom row of Fig. 12(c). The array aperture D is composed of the transmit array aperture D_{T} and the receive array aperture D_{R}. D_{T} represents the distance between the first and the last transmit antennas, i.e., $D_{\mathrm{T}} = x_3 - x_1 = 4\lambda$. By the same token, we can deduce $D_{\mathrm{R}} = y_4 - y_1 = 1.5\lambda$. So the virtual aperture of the 3×4 ULA is $D = D_{\mathrm{T}} + D_{\mathrm{R}} = 4\lambda + 1.5\lambda = 5.5\lambda$, which exactly represents the spacing between the first and the last virtual elements. The normalized array beam pattern is shown in Fig. 13 by the red line. The 3-dB beamwidth of the mainlobe, also known as the Rayleigh angular resolution, is approximately 8.5°. And as expected, the peak sidelobe level is about −13 dB. By increasing the spacing between the virtual elements, we can expand the array aperture, effectively enhancing the Rayleigh angular resolution limit. A MIMO array with non-uniform spacing of these virtual elements is referred to as an $M \times N$ SLA. However, increasing the aperture size may lead to side effects, such as elevated sidelobe levels. Below, we utilize the intrinsic properties of the normalized array beam pattern to explain this.

Let $\xi = \sin(\theta)$, which belongs to $[-1, 1]$. Then the beam pattern in (33) can be expressed as

$$\Phi(\xi) = \frac{1}{L}\left|\sum_{l=1}^{L} e^{-j2\pi z_l \xi/\lambda}\right|. \tag{36}$$

Now we evaluate the integral of the square of $\Phi(\xi)$:

$$\begin{aligned}\int_{-1}^{1} \Phi^2(\xi)\, d\xi &= \frac{1}{L^2}\int_{-1}^{1}\left|\sum_{l=1}^{L} e^{-j2\pi z_l \xi/\lambda}\right|^2 \mathrm{d}\xi \\ &= \frac{1}{L^2}\int_{-1}^{1}\left\{\left[\sum_{l=1}^{L}\cos\left(2\pi\frac{z_l}{\lambda}\xi\right)\right]^2\right. \\ &\qquad \left.+\left[\sum_{l=1}^{L}\sin\left(2\pi\frac{z_l}{\lambda}\xi\right)\right]^2\right\}\mathrm{d}\xi \\ &= \frac{2}{L} + \frac{1}{L^2}\sum_{l\neq l'}\int_{-1}^{1}\left[\cos\left(2\pi\frac{z_l}{\lambda}\xi\right)\cos\left(2\pi\frac{z_{l'}}{\lambda}\xi\right)\right. \\ &\qquad \left.+\sin\left(2\pi\frac{z_l}{\lambda}\xi\right)\sin\left(2\pi\frac{z_{l'}}{\lambda}\xi\right)\right]\mathrm{d}\xi \\ &= \frac{2}{L} + \frac{1}{L^2}\sum_{l\neq l'}\int_{-1}^{1}\cos\left[\frac{2\pi}{\lambda}(z_l - z_{l'})\,\xi\right]\mathrm{d}\xi.\end{aligned} \tag{37}$$

We assume that all the inter-element spacings in the array are integer multiples of half-wavelength, as depicted in Fig. 12. Therefore, we have $z_l - z_{l'} = i\lambda/2$, where $i = 0, \pm1, \pm2, \cdots$ is

an integer. If there are overlapping virtual array elements, i.e., there exists $l \neq l'$ such that $z_l = z_{l'}$, we have

$$\int_{-1}^{1} \cos\left[\frac{2\pi}{\lambda}\left(z_l - z_{l'}\right)\xi\right] \mathrm{d}\xi = 2. \tag{38}$$

For other non-overlapping virtual elements, i.e., $z_l - z_{l'}$ is an non-zero integer multiple of $\lambda/2$, we have

$$\int_{-1}^{1} \cos\left[\frac{2\pi}{\lambda}\left(z_l - z_{l'}\right)\xi\right] \mathrm{d}\xi = \frac{\lambda \sin\left[\frac{2\pi}{\lambda}\left(z_l - z_{l'}\right)\right]}{\pi\left(z_l - z_{l'}\right)}. = 0 \tag{39}$$

Therefore, (37) can be expressed as

$$\int_{-1}^{1} \Phi^2(\xi)\, \mathrm{d}\xi \geq \frac{2}{L}, \tag{40}$$

where the equality holds when there are no overlapping virtual array elements. In other words, the integral of the square of the normalized array beam pattern reaches its minimum value when the virtual elements do not overlap, and this minimum value is inversely proportional to the number of virtual elements. Reduction in the number of antennas, an increase in the number of overlapping virtual elements, and enlargement of the array aperture are all factors that may lead to a higher sidelobe level. Based on this principle, we introduce below a simple and effective array design strategy.

Our first step is to determine an appropriate array aperture size, which should be a positive integer multiple of $\lambda/2$. For an $M \times N$ MIMO array, this means determining the positions of the 2 receive antennas at the edges of the receive array and the 2 transmit antennas at the edges of the transmit array. We partition the apertures of both the receive and transmit arrays into grid points with $\lambda/2$ spacing, and subsequently place the remaining $M-2$ transmit and $N-2$ receive antennas on these equidistant grid points. This ensures that all the inter-element spacings are integer multiples of $\lambda/2$. Then we search exhaustively for all possible MIMO arrays without overlapping virtual elements, and select the one with the lowest sidelobe level. As long as the achieved Rayleigh angular resolution meets our requirements, we choose the array with the lowest sidelobe level as the design outcome. Otherwise, it is necessary to further enlarge the aperture and repeat the above steps.

Based on the above strategy, we proceed to select a 3×4 SLA from the radar board shown in Fig. 12(b). We choose the 9th and 16th receive antennas as the edges of the receive array, i.e., the receive array aperture is $D_{\mathrm{R}} = 3.5\lambda$. And we select the 1st and 12th transmit antennas as the edges of the transmit array, i.e., the transmit array aperture is $D_{\mathrm{T}} = 16\lambda$. So the MIMO array aperture is $D_{\mathrm{V}} = D_{\mathrm{T}} + D_{\mathrm{R}} = 19.5\lambda$. There are 6 elements between the 9th and 16th receive antennas, while there are 10 elements between the 1st and 12th transmit antennas. Since the elevation angle estimation is not considered in this paper, the 4th, 5th and 6th transmit antennas can be ignored. To form the 3×4 SLA, we need to select 2 out of these 6 receive antennas and 1 out of the $10 - 3 = 7$ transmit antennas. Then the number of combinations is

$$\binom{7}{1} \times \binom{6}{2} = 105. \tag{41}$$

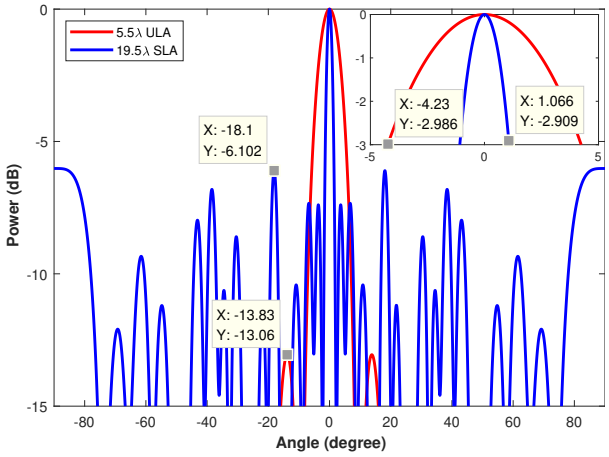

Fig. 13. The normalized beam patterns of different arrays

From the combinations without overlapping virtual elements, we select the one with the lowest sidelobe level, which comprises the 1st, 7th and 12th transmit antennas along with the 9th, 10th, 12th and 16th receive antennas in Fig. 12(b). The position vectors of this 3×4 SLA are listed below:

$$\boldsymbol{x} = [0,\ 6\lambda,\ 16\lambda] \tag{42a}$$

$$\boldsymbol{y} = [0,\ 0.5\lambda,\ 1.5\lambda,\ 3.5\lambda] \tag{42b}$$

and the corresponding beam pattern is shown in Fig. 13 by the blue line. The Rayleigh angular resolution of this array is about 2.1° and the sidelobe level is about -6 dB. By using the IAA type of super-resolution algorithms, the angular resolution of this array can be improved beyond the Rayleigh resolution. In practical situations, factors such as antenna fabrication tolerances and non-ideal signal models can affect the achievable angular resolution, which may deviate from the ideal performance and requires empirical testing. We employ the 3×4 SLA in (42) to develop the ST-CDM MIMO radar prototype.

References

[1] J. Li and P. Stoica, "MIMO Radar with Colocated Antennas," *IEEE Signal Processing Magazine*, vol. 24, no. 5, pp. 106–114, 2007.

[2] ——, *MIMO Radar Signal Processing*, 1st ed. New York: John Wiley & Sons, 2008.

[3] M. Xue, J. Li, and P. Stoica, "MIMO radar waveform design," in *Waveform Design and Diversity for Advanced Radar Systems*. IET Press, 2012, pp. 89–120.

[4] S. Rao, "MIMO Radar," Number SWRA554A, Texas Instruments Inc., Dallas, May 2017.

[5] J. Bechter, F. Roos, and C. Waldschmidt, "Compensation of Motion-Induced Phase Errors in TDM MIMO Radars," *IEEE Microwave and Wireless Components Letters*, vol. 27, no. 12, pp. 1164–1166, 2017.

[6] L. Xu, J. Lien, and J. Li, "Doppler–Range Processing for Enhanced High-Speed Moving Target Detection Using LFMCW Automotive Radar," *IEEE Transactions on Aerospace and Electronic Systems*, vol. 58, no. 1, pp. 568–580, 2022.

[7] H. Sun, F. Brigui, and M. Lesturgie, "Analysis and comparison of MIMO radar waveforms," in *2014 International Radar Conference*, Lille, France, October 2014, pp. 1–6.

[8] X. Shang and Y. Cheng, "Code Optimization and Angle-Doppler Imaging for ST-CDM LFMCW MIMO Radar Systems," *IEEE Signal Processing Letters*, vol. 29, pp. 2043–2047, 2022.

[9] A. Moffet, "Minimum-redundancy linear arrays," *IEEE Transactions on Antennas and Propagation*, vol. 16, no. 2, pp. 172–175, 1968.

[10] W. Roberts, L. Xu, J. Li, and P. Stoica, "Sparse Antenna Array Design for MIMO Active Sensing Applications," *IEEE Transactions on Antennas and Propagation*, vol. 59, no. 3, pp. 846–858, 2011.

[11] "AWR2243 Evaluation Module (AWR2243BOOST) mmWave Sensing Solution," Number SPRUIT8D, Texas Instruments Incorporated, Dallas, February 2020.

[12] "AWR2243 Single-Chip 76- to 81-GHz FMCW Transceiver," Number SWRS223B, Texas Instruments Incorporated, Dallas, February 2020.

[13] P. Wang, P. Boufounos, H. Mansour, and P. V. Orlik, "Slow-Time MIMO-FMCW Automotive Radar Detection with Imperfect Waveform Separation," in *ICASSP 2020 - 2020 IEEE International Conference on Acoustics, Speech and Signal Processing (ICASSP)*, Barcelona, Spain, May 2020, pp. 8634–8638.

[14] R. Lin, G. Wang, and J. Li, "On the design of linear sparse arrays with beampattern shift invariant properties," *Signal Processing*, vol. 199, p. 108632, 2022.

[15] T. Yardibi, J. Li, P. Stoica, M. Xue, and A. B. Baggeroer, "Source Localization and Sensing: A Nonparametric Iterative Adaptive Approach Based on Weighted Least Squares," *IEEE Transactions on Aerospace and Electronic Systems*, vol. 46, no. 1, pp. 425–443, 2010.

[16] W. Roberts, P. Stoica, J. Li, T. Yardibi, and F. A. Sadjadi, "Iterative Adaptive Approaches to MIMO Radar Imaging," *IEEE Journal of Selected Topics in Signal Processing*, vol. 4, no. 1, pp. 5–20, 2010.

[17] M. Xue, L. Xu, and J. Li, "IAA Spectral Estimation: Fast Implementation Using the Gohberg-Semencul Factorization," *IEEE Transactions on Signal Processing*, vol. 59, no. 7, pp. 3251–3261, 2011.

[18] S. Sun, A. P. Petropulu, and H. V. Poor, "MIMO Radar for Advanced Driver-Assistance Systems and Autonomous Driving: Advantages and Challenges," *IEEE Signal Processing Magazine*, vol. 37, no. 4, pp. 98–117, 2020.

[19] A. Cohen, L. Maor, M. Teplitsky, and I. Yoffe, "Beamforming techniques implementing the iterative adaptive approach (IAA)," U.S. Patent 11,532,883 B2, December 20, 2022.

[20] F. Robey, "Beyond Linear Processing (BLiP)," darpa.mil, October 2022. [Online]. Available: https://www.darpa.mil/program/beyond-linear-processing

[21] J. Li, "Over a Century of Array Signal Processing," ieee-aess.org, March 2023. [Online]. Available: https://ieee-aess.org/presentation/lecture/over-century-array-signal-processing

[22] H. Liu, X. Shang, and R. Lin, "Automotive ST-CDM MIMO Radar Imaging," in *2023 20th European Radar Conference (EuRAD)*, Berlin, Germany, September 2023, pp. 205–208.

[23] P. Stoica, P. Babu, and J. Li, "New Method of Sparse Parameter Estimation in Separable Models and Its Use for Spectral Analysis of Irregularly Sampled Data," *IEEE Transactions on Signal Processing*, vol. 59, no. 1, pp. 35–47, 2011.

[24] ——, "SPICE: A Sparse Covariance-Based Estimation Method for Array Processing," *IEEE Transactions on Signal Processing*, vol. 59, no. 2, pp. 629–638, 2011.

[25] P. Stoica and P. Babu, "SPICE and LIKES: Two hyperparameter-free methods for sparse-parameter estimation," *Signal Processing*, vol. 92, no. 7, pp. 1580–1590, 2012.

[26] X. Tan, W. Roberts, J. Li, and P. Stoica, "Sparse Learning via Iterative Minimization With Application to MIMO Radar Imaging," *IEEE Transactions on Signal Processing*, vol. 59, no. 3, pp. 1088–1101, 2011.

[27] "Imaging Radar Using Cascaded mmWave Sensor Reference Design," Number TIDUEN5A, Texas Instruments Incorporated, Dallas, June 2019.

[28] X. Zhang, Z. Liu, Y. Kong, and C. Li, "Mutual Interference Suppression Using Signal Separation and Adaptive Mode Decomposition in Noncontact Vital Sign Measurements," *IEEE Transactions on Instrumentation and Measurement*, vol. 71, pp. 1–15, 2022.

[29] G. Li, Y. Ge, Y. Wang, Q. Chen, and G. Wang, "Detection of Human Breathing in Non-Line-of-Sight Region by Using mmWave FMCW Radar," *IEEE Transactions on Instrumentation and Measurement*, vol. 71, pp. 1–11, 2022.

[30] Y. Ma, H. Hong, K. Xue, H. Zhao, C.-H. Fu, C. Gu, Y. Zhang, and X. Zhu, "Multitarget Time-Varying Vocal Folds Vibration Detection Using MIMO FMCW Radar," *IEEE Transactions on Instrumentation and Measurement*, vol. 71, pp. 1–12, 2022.

[31] Z. Xu, S. Qi, and P. Zhang, "A Coherent CZT-Based Algorithm for High-Accuracy Ranging With FMCW Radar," *IEEE Transactions on Instrumentation and Measurement*, vol. 72, pp. 1–11, 2023.

[32] R. Schmidt, "Multiple emitter location and signal parameter estimation," *IEEE Transactions on Antennas and Propagation*, vol. 34, no. 3, pp. 276–280, 1986.

[33] G. Bienvenu, "Influence of the spatial coherence of the background noise on high resolution passive methods," in *ICASSP '79. IEEE International Conference on Acoustics, Speech, and Signal Processing*, vol. 4, Washington, DC, USA, April 1979, pp. 306–309.

[34] S. Bagchi and S. K. Mitra, *The nonuniform discrete Fourier transform and its applications in signal processing*, 1st ed. New York: Springer Science & Business Media, 2012, vol. 463.